J. Fluid Mech. (2010), *vol.* 651, *pp.* 503–518. © Cambridge University Press 2010
doi:10.1017/S0022112010000145

Vortex shedding from a submerged rectangular obstacle attacked by a solitary wave

MENG-YU LIN† AND LIANG-HSIUNG HUANG

Department of Civil Engineering, National Taiwan University, Taipei 106, Taiwan, ROC

(Received 15 November 2008; revised 5 January 2010; accepted 5 January 2010;
first published online 29 March 2010)

This study investigates the two-dimensional flow of a solitary wave that passes over a submerged rectangular obstacle using a Lagrangian-type numerical method. The main purpose is to investigate vortex generation and evolution caused by the obstacle. The numerical method is based on the combination of vortex methods and boundary integral methods using the Helmholtz decomposition. The simulated flow pattern is compared with the experimental measurements in detail, and the overall agreement is reasonably good. A series of simulations were performed with various wave heights to study the effect of wave height on vortex generation and evolution. The relation between the vorticity field and the drag experienced by the obstacle is also discussed. In the presented cases, the effects of the generated vortices are preserved over a long period, and may cause local scouring of the foundation at the lee side of the obstacle. The deformation of the solitary wave is not much affected by the presence of the vortices, but the drag is significantly affected by the vorticity field. An almost linear relationship between the Reynolds number and the maximum magnitude of the drag (positive and negative) is observed.

1. Introduction

Wave-structure interaction is a classical subject in water wave mechanics. This subject is closely associated with issues in coastal engineering, such as the construction of submerged breakwaters to dissipate wave energy or to retard the offshore movement of sand. The occurrence of scouring around breakwaters is also an important area of research because it is one of the major failure modes of these structures. In the past, although scour at emerged breakwaters has been studied fairly extensively, very little is known about scour at/around submerged breakwaters (Sumer *et al.* 2005). For example, Sánchez-Arcilla and his co-workers conducted the experimental investigations on the scouring caused by the wave field over/through/around the trunk section of submerged structure (Gironella & Sánchez-Arcilla 1999; Sánchez-Arcilla *et al.* 2000). Sumer *et al.* (2005) conducted a systematic experimental study of scour around low-crested structures/submerged breakwaters, for both the two-dimensional trunk section scour and the three-dimensional roundhead scour.

Many studies of flows of surface waves and submerged obstacles have been performed using potential flow theory based on the assumption that the flow is irrotational (e.g. Mei & Black 1969; Baker, Meiron & Orszag 1989; Grue 1992; Yeung & Vaidhyanathan 1992; Grilli, Losada & Martin 1994; Guyenne & Nicholls 2005). However, flow separation should not be neglected in the study of the flow field

† Email address for correspondence: mylin@mac.com

https://doi.org/10.1017/S0022112010000145 Published online by Cambridge University Press

around submerged bodies. Consequently, several researchers have studied this problem by solving the Navier–Stokes equations for laminar flows or the Reynolds-averaged Navier–Stokes equations with turbulence closure for turbulent flows, using various numerical approaches, including finite difference methods (e.g. Zhang & Chwang 1999; Chang, Hsu & Liu 2001), finite analytic methods (e.g. Tang & Chang 1998; Sue, Chern & Hwang 2005), finite volume methods (e.g. Hsu, Hsieh & Hwang 2004) and finite element methods (e.g. Idelsohn, Onate & Sacco 1999; Lo & Young 2004). These are all grid-based schemes, and may not be capable of simulating the complex vortex structures if the grid resolution in the vortical regions is not sufficiently fine (see Lin *et al.* 2006).

Lin & Huang (2009) developed a numerical scheme that combines vortex methods and boundary integral methods via the Helmholtz decomposition to study the generation and evolution of the vortices in water waves that propagate over a submerged structure. The major advantages of this approach are the capacity of boundary integral methods to capture the motion of the free surface and the essentially grid-free nature of vortex methods in simulating the complex vortex structures in compact regions. Their numerical model was confirmed by simulating periodic waves that move over a submerged rectangular obstacle using non-uniform vortex blobs with mapping of the redistribution lattice. Moreover, their computations neglected the generation of vorticity on the sea-floor.

This study extends the work of Lin & Huang (2009) to the simulation of solitary waves travelling over a submerged rectangular obstacle. In the computations in this study, the vortex method with uniform blob size is employed, because for a solitary wave the generated vortices are not confined in the regions close to the corners of the obstacle. Additionally, the process of creation of vorticity at the sea-floor is considered because it plays an important role in the formation of vortices. First, to validate the numerical model, the experiment conducted by Lin *et al.* (2006, referred to as LCHC from here on) is reproduced. In this calculation case, the process of the generation and evolution of vortices is also studied in detail. Then, the effect of wave height on the strength of vortices is investigated, and the effects of the vortices on the wave deformation and the drag coefficient are also discussed.

2. Description of flow problem

The problem of interest concerns the calculation of the two-dimensional flow of a solitary wave over a submerged rectangular obstacle in a uniform channel. Since for most problems in water wave mechanics the free-surface viscosity is negligible, the generation of vorticity on the free surface can be neglected. A Cartesian coordinate system is fixed such that the x-axis lies in the undisturbed free surface and the y-axis points vertically upward (see figure 1, the image part will be introduced later). Incompressible flow with constant density and viscosity is considered, and the motion of the fluid can be determined using the vorticity transport equation,

$$\frac{\mathrm{D}\omega}{\mathrm{D}t} = \frac{\partial \omega}{\partial t} + \boldsymbol{u}\cdot\nabla\omega = \nu\nabla^2\omega, \tag{2.1}$$

where $\boldsymbol{u}$ is the velocity field, ν is the molecular viscosity, and $\omega = \hat{\boldsymbol{k}}\cdot\nabla\times\boldsymbol{u}$ is the vorticity field with the unit vector $\hat{\boldsymbol{k}}$ out of the page.

https://doi.org/10.1017/S0022112010000145 Published online by Cambridge University Press

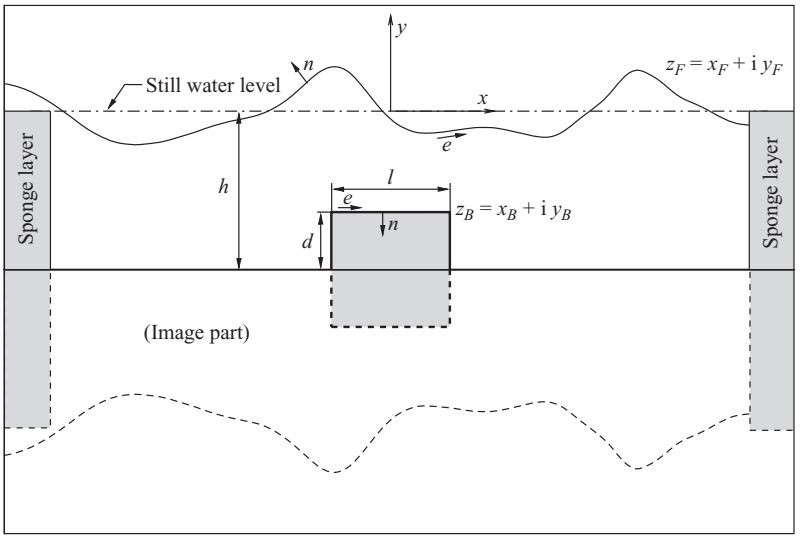


FIGURE 1. Definition sketch for water waves over a submerged obstacle.

On the free surface, the flow field satisfies the kinematic and dynamic boundary conditions,

$$\frac{\mathrm{D}\boldsymbol{x}_F}{\mathrm{D}t} = \boldsymbol{u}(\boldsymbol{x}_F) \tag{2.2}$$

and

$$\frac{\mathrm{D}\boldsymbol{u}}{\mathrm{D}t}(\boldsymbol{x}_F) = -\frac{1}{\rho}\nabla p_a - g\nabla(\boldsymbol{x}_F \cdot \hat{\boldsymbol{j}}), \tag{2.3}$$

respectively, where $\boldsymbol{x}_F$ represents the free-surface points, p_a is the pressure at the free surface and $\hat{\boldsymbol{j}}$ is the unit vector pointing vertically upward. The no-slip boundary condition is imposed at the surface of the obstacle and on the bottom of the channel (the sea-floor). At the lateral boundaries, numerical sponge layers (cf. Baker *et al.* 1989) are set to truncate the computational domain into a limited region and to absorb the outwardly travelling waves.

3. Outline of numerical method

The numerical model employed herein is based on the scheme of Lin & Huang (2009). Since the details of the model are lengthy, this section presents only an outline.

Applying the integral formulations of the Helmholtz decomposition (see Morino 1990) yields the integral representation for the velocity field:

$$\boldsymbol{u}(\boldsymbol{x}) = \int_V \omega(\boldsymbol{x}')\hat{\boldsymbol{k}} \times \nabla G \,\mathrm{d}\boldsymbol{x}' + \int_{S_F} \Gamma_F(\boldsymbol{x}')\hat{\boldsymbol{k}} \times \nabla G \,\mathrm{d}\boldsymbol{x}', \tag{3.1}$$

where S_F denotes the free surface; Γ_F is the strength of a vortex sheet that is induced by the jump in tangential velocity across the free surface and G is the fundamental solution of Laplace's equation given by

$$G = G(\boldsymbol{x}, \boldsymbol{x}') = \frac{1}{2\pi}\ln|\boldsymbol{x} - \boldsymbol{x}'|. \tag{3.2}$$

https://doi.org/10.1017/S0022112010000145 Published online by Cambridge University Press

From this integral formulation, an alternative problem may be constructed for solving $\boldsymbol{x}_F$, Γ_F and ω rather than the original problem with primitive variables. The vorticity field ω is determined by applying vortex methods to obtain a numerical approximation in terms of N vorticity-carrying particles

$$\omega(\boldsymbol{x}, t) = \sum_{j=1}^{N} \eta(\boldsymbol{x} - \boldsymbol{x}_j(t))\Gamma_j(t) \tag{3.3}$$

with their circulation Γ_j and distribution function η. In this work, a Gaussian distribution is used:

$$\eta(\boldsymbol{x}) = \frac{1}{2\pi\epsilon^2} \exp\left(-\frac{|\boldsymbol{x}|^2}{2\epsilon^2}\right), \tag{3.4}$$

where the quantity ϵ is the core size of the vortex particles. According to (2.1), the transport of vorticity is solved by convecting the particles in a Lagrangian frame and accounting for viscous effects by changing their strength. In this work, viscous effects are simulated using the method of particle-strength exchange (Degond & Mas-Gallic 1989).

The free-surface points $\boldsymbol{x}_F$ and the strength of the vortex sheet Γ_F are determined by imposing the free-surface boundary conditions. Additionally, to determine the vorticity flux at the solid boundary, a spurious vortex sheet on S_B is obtained by imposing the no-penetration boundary condition. For convenience, the complex notation $z = x + \mathrm{i}y$ is used for the complex field point and $q = u + \mathrm{i}v$ represents the complex velocity, where q is not an analytic function. The kinematic and dynamic free-surface boundary conditions, (2.2) and (2.3), respectively, and the no-penetration boundary condition on the surface of the obstacle can be expressed as

$$\frac{\partial z_F}{\partial t}(e, t) = q_F(e) + \frac{\alpha\gamma_F}{2(z_F^*)_e}, \tag{3.5}$$

$$\frac{\partial \gamma_F}{\partial t} = -2\left[\mathrm{Re}\left\{\frac{\partial q_F^*}{\partial t}(z_F)_e - \frac{\alpha\gamma_F}{2}\frac{(q_F)_e}{(z_F)_e}\right\} + g(y_F)_e\right] + \left(\frac{\alpha}{2} - \frac{1}{4}\right)\frac{\partial}{\partial e}\frac{\gamma_F^2}{(z_F)_e(z_F^*)_e}, \tag{3.6}$$

$$\frac{\partial \gamma_B}{\partial t} = 2\mathrm{Re}\left\{(z_B)_e \frac{\partial q_B^*}{\partial t}\right\}, \tag{3.7}$$

where e is the Lagrangian variable along the boundaries, $(\,)_e$ denotes differentiation with respect to the label e and the asterisk indicates complex conjugate. γ_F is the non-normalized strength of the vortex sheet at the free surface, given by $\gamma_F(e) = \Gamma_F(e)|(z_F)_e|$; γ_B represents the spurious vortex sheet on S_B; q_F and q_B are the principal-value velocity on the free surface and the solid boundary, respectively, and given by

$$q_F^*(e) = \frac{1}{2\pi\mathrm{i}}\fint_{S_F} \frac{\gamma_F(e')}{z_F(e) - z_F(e')}\,\mathrm{d}e' + \frac{1}{2\pi\mathrm{i}}\int_{S_B} \frac{\gamma_B(e')}{z_F(e) - z_B(e')}\,\mathrm{d}e' \frac{1}{2\pi\mathrm{i}}\sum_{j=1}^{N}\frac{\Gamma_j}{z_F(e) - z_j}, \tag{3.8}$$

$$q_B^*(e) = \frac{1}{2\pi\mathrm{i}}\int_{S_F} \frac{\gamma_F(e')}{z_B(e) - z_F(e')}\,\mathrm{d}e' + \frac{1}{2\pi\mathrm{i}}\fint_{S_B} \frac{\gamma_B(e')}{z_B(e) - z_B(e')}\,\mathrm{d}e' + \frac{1}{2\pi\mathrm{i}}\sum_{j=1}^{N}\frac{\Gamma_j}{z_B(e) - z_j}. \tag{3.9}$$

https://doi.org/10.1017/S0022112010000145 Published online by Cambridge University Press

Equation (3.5) is used to determine the Lagrangian motion of the free-surface position $\boldsymbol{x}_F$. The velocity of these Lagrangian points is a weighted average of the velocities across the free surface, chosen by the weighting factor α ($|\alpha| \leqslant 1$).

The evolution equations for γ_F and γ_B, (3.6) and (3.7), respectively, are coupled Fredholm integral equations of the second kind, and can therefore be efficiently solved using an iteration algorithm (see Baker, Meiron & Orszag 1982 for more details). To determine efficiently the vortex flux on the bottom of the channel, the method of image is employed (as presented in the lower part of figure 1) such that the no-penetration condition is automatically fulfilled, and the spurious slip velocity is then turned into the vorticity flux (see Koumoutsakos, Leonard & Pépin 1994). The vorticity creation from solid boundaries (the surface of the obstacle and the bottom of the channel) is performed by distributing vorticity flux to neighbouring particles. In this study, the approximate solution proposed by Ploumhans & Winckelmans (2000) to determine the increasing rate of the circulation of particles due to the vorticity flux is used. An artificial viscosity model (Cottet 1996), regarded as an eddy viscosity model in vortex methods, is adopted to cancel the contribution from the antidiffusive part of the truncation error involved in vortex computations. A particle redistribution scheme (see Lin & Huang 2009) is applied every five time steps to ensure a good overlap of the core sizes of the particles. In the redistribution procedure, the overlap ratio (defined as the inter-particle spacing divided by the particle size) is set equal to one. A fourth-order Adams–Bashforth–Moulton predictor-corrector scheme is utilized to perform the time integrations for $\partial\gamma_F/\partial t$ and $\partial\gamma_B/\partial t$ (fourth-order Runge–Kutta technique for the first few time steps). The time marching of the positions of vortex particles is performed using a second-order Adams–Bashforth scheme (second-order Runge–Kutta for the first step and after each redistribution).

4. Calculation of drag coefficient

The drag force $\boldsymbol{F}_D$ is computed as the sum of the pressure drag and the friction drag:

$$\boldsymbol{F}_D = \rho\,\hat{\boldsymbol{i}} \cdot \left\{ \int_{S_B} p\,\hat{\boldsymbol{n}}\,\mathrm{d}S + \nu \int_{S_B} \hat{\boldsymbol{n}} \times (\omega\hat{\boldsymbol{k}})\,\mathrm{d}S \right\}, \tag{4.1}$$

and the drag coefficient c_D on the obstacle is then given by

$$c_D = \frac{\boldsymbol{F}_D \cdot \hat{\boldsymbol{i}}}{\frac{1}{2}\rho g[h^2 - (h-d)^2]}. \tag{4.2}$$

In (4.1), the friction drag can be computed directly from the vorticity on the surface of the obstacle. The pressure field may be obtained by solving the pressure Poisson equation

$$\nabla^2 B = \nabla \cdot (\boldsymbol{u} \times (\omega\hat{\boldsymbol{k}})), \tag{4.3}$$

where B is the so-called total pressure defined as

$$B = \frac{p}{\rho} + \frac{|\boldsymbol{u}|^2}{2} + gy. \tag{4.4}$$

The pressure on the surface of the obstacle is determined using the integral equation formulation derived from (4.3) (see Uhlman 1992):

$$\frac{1}{2}B - \int_S B\frac{\partial G}{\partial n}\,\mathrm{d}\boldsymbol{x}' = \int_V \nabla G \cdot (\omega\hat{\boldsymbol{k}} \times \boldsymbol{u})\,\mathrm{d}\boldsymbol{x}' + \int_S \left\{ G\hat{\boldsymbol{n}} \cdot \frac{\partial \boldsymbol{u}}{\partial t} + \nu\nabla G \cdot (\hat{\boldsymbol{n}} \times \hat{\boldsymbol{k}})\omega \right\} \mathrm{d}\boldsymbol{x}'. \tag{4.5}$$

https://doi.org/10.1017/S0022112010000145 Published online by Cambridge University Press

Case No.	H/h	d/h	l/h	h	U	Re (Uh/ν)
1	0.17	3/7	6/7	0.07	0.27	1.88×10^4
2	0.3	3/7	6/7	0.07	0.50	3.47×10^4
3	0.4	3/7	6/7	0.07	0.69	4.80×10^4
4	0.5	3/7	6/7	0.07	0.89	6.22×10^4

TABLE 1. Conditions for the calculation cases.

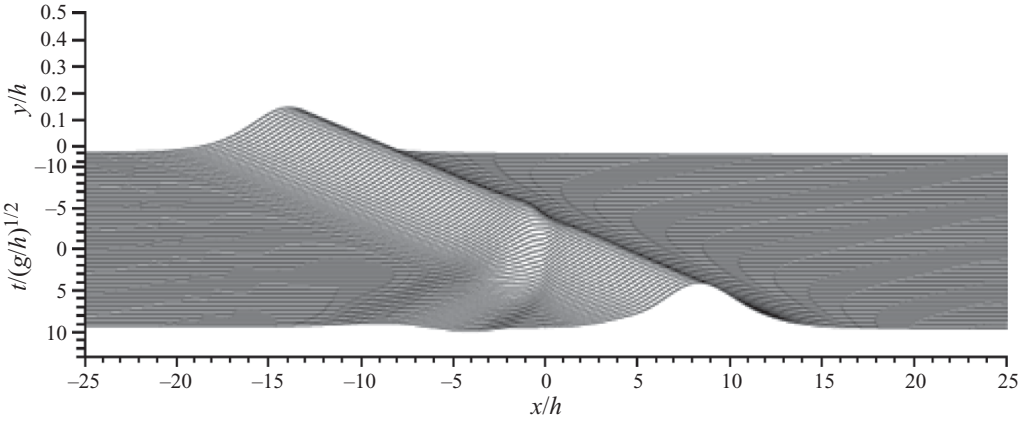


FIGURE 2. Free-surface profiles at various times for $H/h = 0.17$.

5. Results and discussion

This section presents the computational results concerning the flow around a submerged rectangular obstacle that is attacked by a solitary wave. Computations are performed for various values of H/h, where H is the incident wave height and h is the still water depth. The case of $H/h = 0.17$ is considered first to validate the presented numerical method and provide some insight into the processes of unsteady separation and vortex shedding that occur in such flows. The computations are non-dimensionalized by the still water depth h and the linear long-wave phase speed $\sqrt{gh}$.

In all computations, a channel with domain $-25 \leqslant x/h \leqslant 25$ and a rectangular obstacle with height $d/h = 3/7$ and length $l/h = 6/7$ are used. The centre of the obstacle is located at $x = 0$. Sponge layers are placed at $-25 \leqslant x/h \leqslant -24.5$ and $24.5 \leqslant x/h \leqslant 25$. In all runs, 870 panels on the free surface and 400 panels on the boundary of the obstacle are used. The initial wave profile is obtained using Tanaka's method (Tanaka 1986), which can determine the exact solitary wave solution. Table 1 summarizes the conditions of the computations presented herein. The Reynolds number (Re) is evaluated based on the depth-averaged velocity (U) under the wave crest and above the obstacle, which is estimated by the following formula (see Chang, Hsu & Liu 2005):

$$U = \frac{H}{h-d}\sqrt{g(h+H)}.$$

5.1. *Generation and evolution of vorticity in the case* $H/h = 0.17$

Figure 2 presents the free-surface profiles at various times obtained from the numerical results for case 1. Here, $t = 0$ represents the moment when the wave crest arrives at

https://doi.org/10.1017/S0022112010000145 Published online by Cambridge University Press

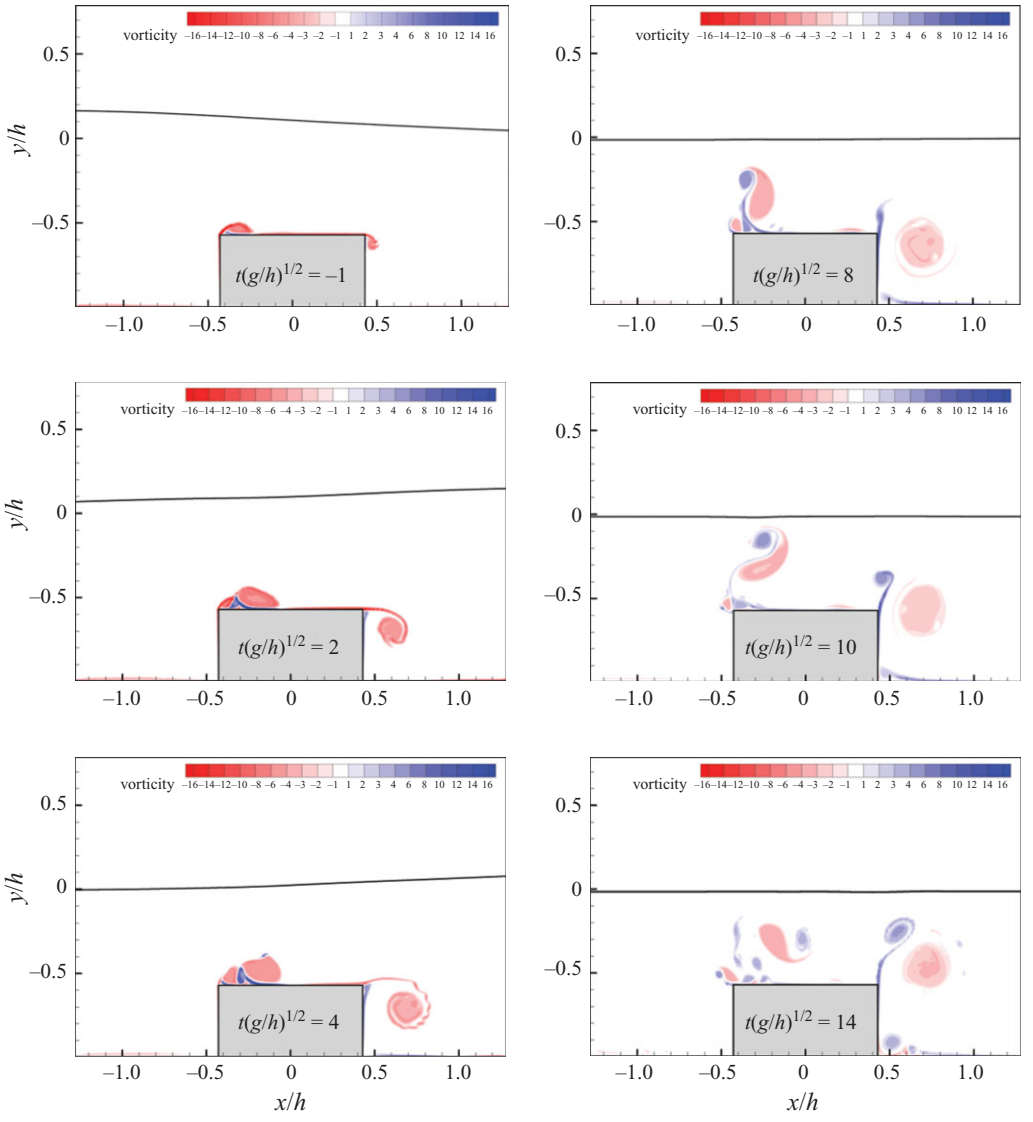


FIGURE 3. Evolution of the vorticity field for $H/h = 0.17$.

the leading edge of the obstacle. One may observe the weak deformation of the transmitted wave and the reflected waves with relatively small amplitudes. Figure 3 presents the evolution of the vorticity field in which the magnitude of vorticity is non-dimensionalized by h in length and $\sqrt{gh}$ in celerity. As expected, small vortices are formed when the wave crest approaches the obstacle. When the wave crest passes through the obstacle, the vortices are convected downstream, grow in size and induce strong secondary vorticity. A Kelvin–Helmholtz-type instability in the separating shear layer from the trailing edge appears at time $t\sqrt{g/h} \approx 4$. As the flow field gradually becomes dominated by vorticity, the lee-side vortex moves upward and interferes with the shedding process at the trailing edge of the obstacle. Accordingly, the newly generated separating shear layer rolls up counterclockwise and then pairs up with the upward-moving vortex to form a dipolar structure. Since the clockwise

https://doi.org/10.1017/S0022112010000145 Published online by Cambridge University Press

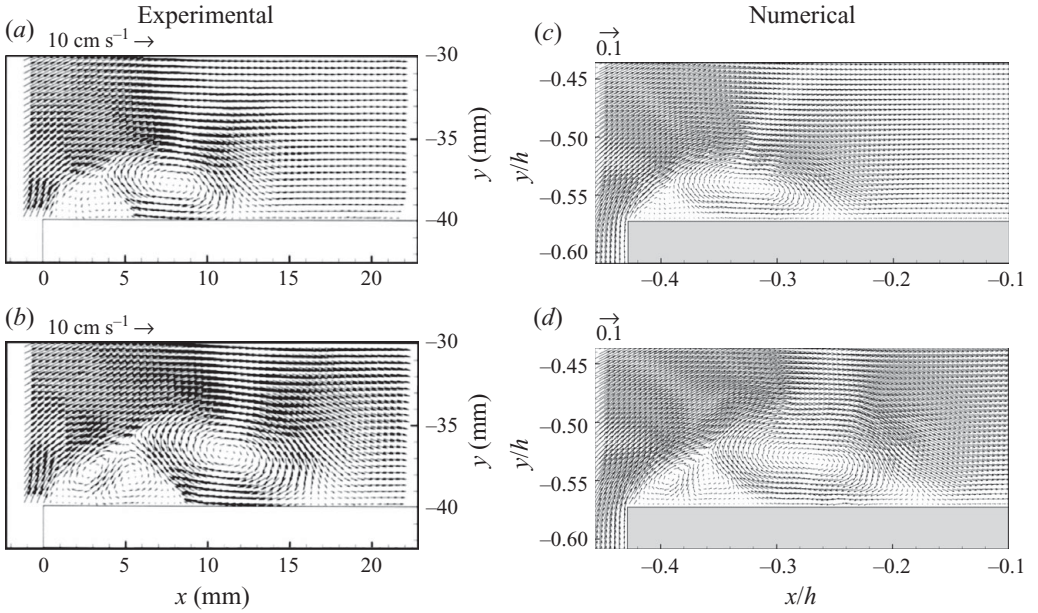


FIGURE 4. Comparison of the velocity fields at the leading edge of the obstacle between the experimental measurements by LCHC (*a*, *b*) and the numerical results for $H/h = 0.17$ (*c*, *d*). (*a*) $t\sqrt{g/h} = -2.37$, (*b*) $t\sqrt{g/h} = -1.18$, (*c*) $t\sqrt{g/h} = -2.4$ and (*d*) $t\sqrt{g/h} = -1.2$.

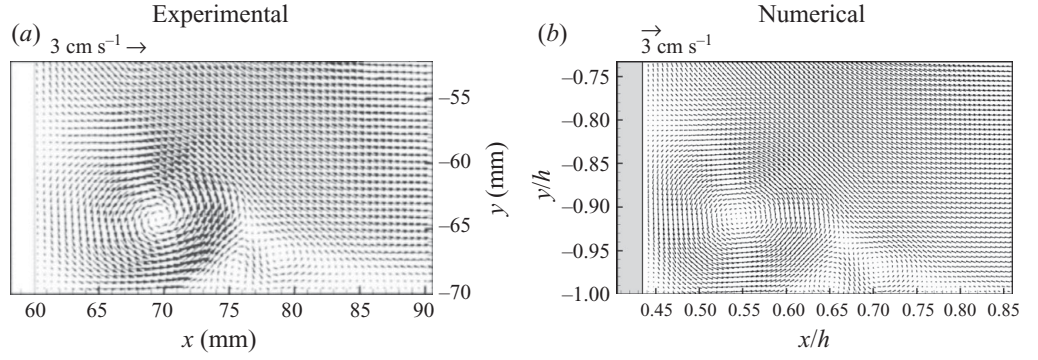


FIGURE 5. Comparison of the velocity fields near the sea-floor at the lee side of the obstacle between (*a*) the experimental measurements by LCHC (at $t\sqrt{g/h} = 12.43$) and (*b*) the numerical results for $H/h = 0.17$ (at $t\sqrt{g/h} = 12.5$).

vortex has more circulation than the other, the dipole moves off to the right along a curved trajectory. Meanwhile, at the lee side of the obstacle, a small vortex is formed at the sea-floor.

LCHC performed an experimental study of this flow for $h = 0.07$ m using laser-induced fluorescence (LIF) and particle image velocimetry (PIV) systems. Figures 4 and 5 compare the local velocity field computed by the presented model with that measured by LCHC. It is evident that the numerical results exhibit features of the complicated vortex structures and agree quite closely with the experimental observations. Figure 6 presents the evolution of the global flow pattern obtained by LCHC. Note that the leading-edge vortices cannot be presented clearly because

https://doi.org/10.1017/S0022112010000145 Published online by Cambridge University Press

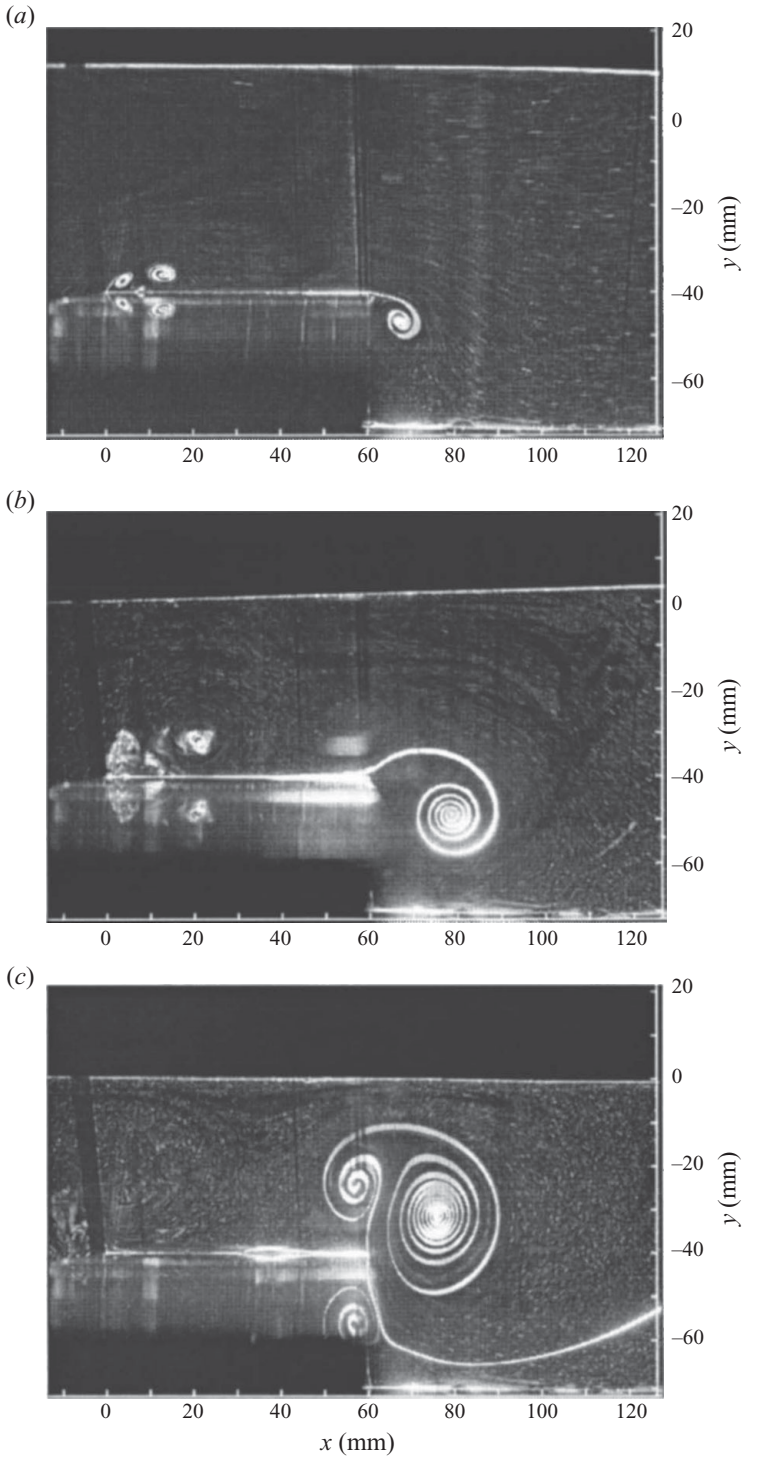


FIGURE 6. Global flow pattern obtained by LCHC using LIF at (*a*) $t\sqrt{g/h} = -0.95$, (*b*) $t\sqrt{g/h} = 2.01$ and (*c*) $t\sqrt{g/h} = 13.97$.

https://doi.org/10.1017/S0022112010000145 Published online by Cambridge University Press

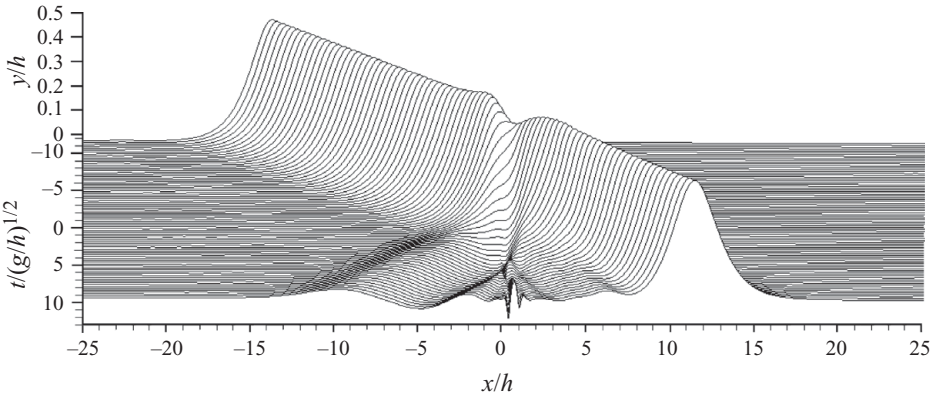


FIGURE 7. Free-surface profiles at various times for $H/h = 0.5$.

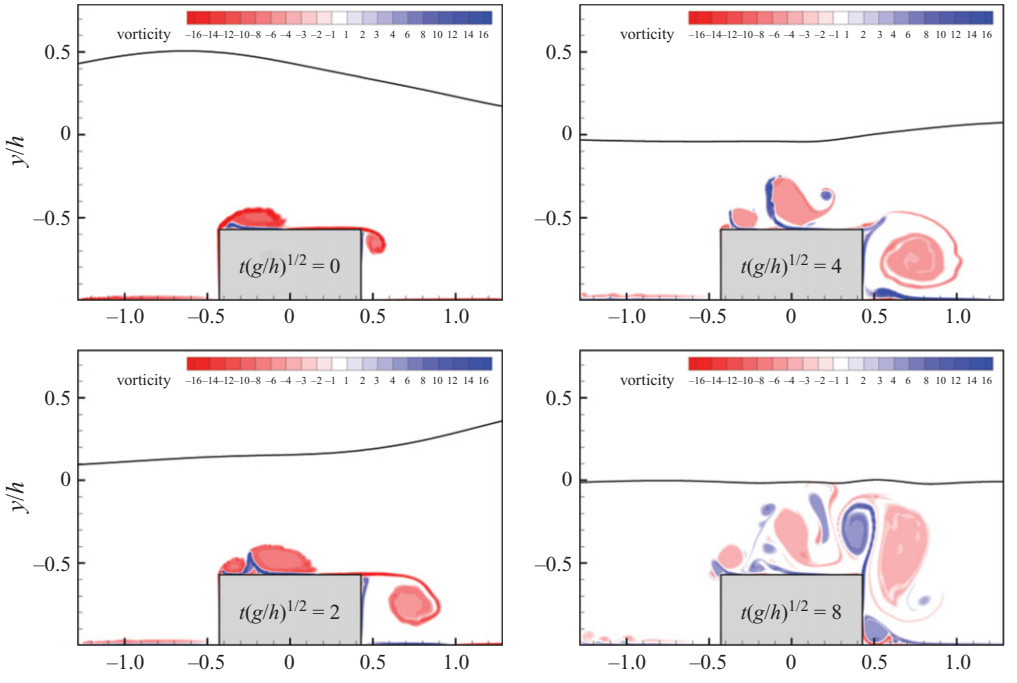


FIGURE 8. Evolution of the vorticity field for $H/h = 0.5$.

turbulent mixing diluted the fluorescent dye. One may observe that the computational results agree satisfactorily with the observations made in the laboratory, except when the lee-side vortex pair is close to the free surface. This fact is attributable to the accumulation of numerical errors in the computations. However, it may also be reasonably attributed to experimental errors caused by the weak reflection of waves from the end of the wave tank.

5.2. *Effects of wave height on vortex generation*

To study the effects of the wave height on the generation and evolution of vortices, further calculations are made for $H/h = 0.3$, 0.4 and 0.5. As an example, figures 7 and 8 plot the evolution of the free-surface profile and the vorticity field for $H/h = 0.5$. As

https://doi.org/10.1017/S0022112010000145 Published online by Cambridge University Press

expected, when the wave height H is larger, the strength of the resulting vortices is greater and their effects stronger. For example, a significant vortex that is formed near the sea-floor at the lee side of the obstacle and a local disturbance of the free surface that is caused by the approach of the lee-side vortex pair may be observed. The results suggest that the formation of the lee-side vortices may cause the scouring of the seabed around coastal structures. Notably, since the vortical flow structure in the case $H/h = 0.5$ becomes very complicated, three-dimensional effects may occur in reality.

In figure 9, the evolution of the wave profiles in all cases, which is computed using the presented model, is compared with the potential-flow result that is computed under the assumption that the flow is inviscid and irrotational. The results reveal that the free-surface displacement that is caused by the vortices is positively correlated with the incident wave height, mainly because of the bulge of the leading-edge vortices, which changes the effective boundary of the flow above the submerged body.

Because the evolution of the minimum value of the stream function (ψ_c) in the core of the lee-side vortex is useful in monitoring the development of the vortex (as an example, figure 10 shows the evolution of the instantaneous streamlines for $H/h = 0.17$), the time histories of $|\psi_c|$ for different wave heights are plotted in figure 11. These curves follow a similar trend: the lee-side vortex reaches its strongest state when the wave crest has left the obstacle and the vortices have begun to dominate the flow field. Figure 12 plots the maximum value of $|\psi_c|$ as a function of Re. Since Re depends linearly on H/h, a nearly linear relationship between the maximum value of $|\psi_c|$ and Re is presented.

5.3. *Drag coefficient*

In figure 13, the drag coefficients that are computed using the present model and by the potential-flow version of the model in each case are presented together. These curves are similar in that they reach their positive maximum when the wave crest approaches the leading edge of the obstacle and then decline gradually to a negative value as the wave crest passes through the obstacle. Since the vortices act to 'pull' the obstacle in the positive x-direction, the negative maximum of the drag is much less than its positive maximum. In contrast, the drag determined from the potential-flow model is almost symmetric because it is caused only by the displacement of the water surface and the solitary wave is almost preserved. Additionally, an almost linear relationship between Re and the maximum drag coefficient (positive and negative) is observed, as presented in figure 14.

6. Concluding remarks

A Lagrangian-type numerical scheme that combines boundary integral methods with vortex methods by the Helmholtz decomposition was adopted to investigate numerically a solitary wave that passes over a submerged rectangular obstacle. The details of the generation and evolution of the vortices caused by flow separation from the obstacle are studied. In this problem, the separating shear layers that cause the generation of vortices are confined inside small regions around the submerged obstacle. The presented model is capable of simulating the separation of shear layers, as the vorticity-carrying elements automatically adjust to such regions. In contrast, in grid-based simulations, vortices may decay too rapidly because of numerical dissipation if the grid resolution in the vortical regions is not sufficiently fine.

https://doi.org/10.1017/S0022112010000145 Published online by Cambridge University Press

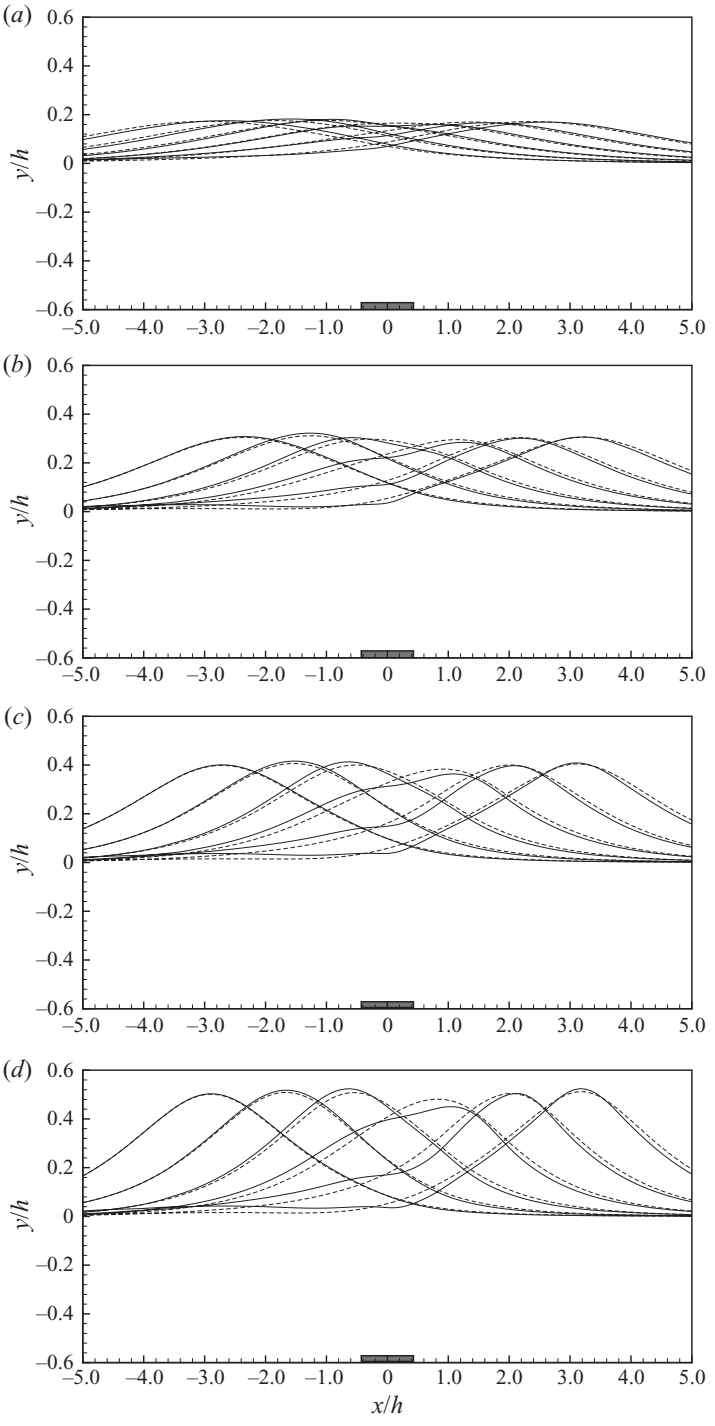


FIGURE 9. Free-surface profile at $t\sqrt{g/h} = -2, -1, 0, 1, 2, 3$, as computed by the present model (——) and by the potential-flow model (- - -). (*a*) $H/h = 0.17$, (*b*) $H/h = 0.3$, (*c*) $H/h = 0.4$ and (*d*) $H/h = 0.5$.

https://doi.org/10.1017/S0022112010000145 Published online by Cambridge University Press

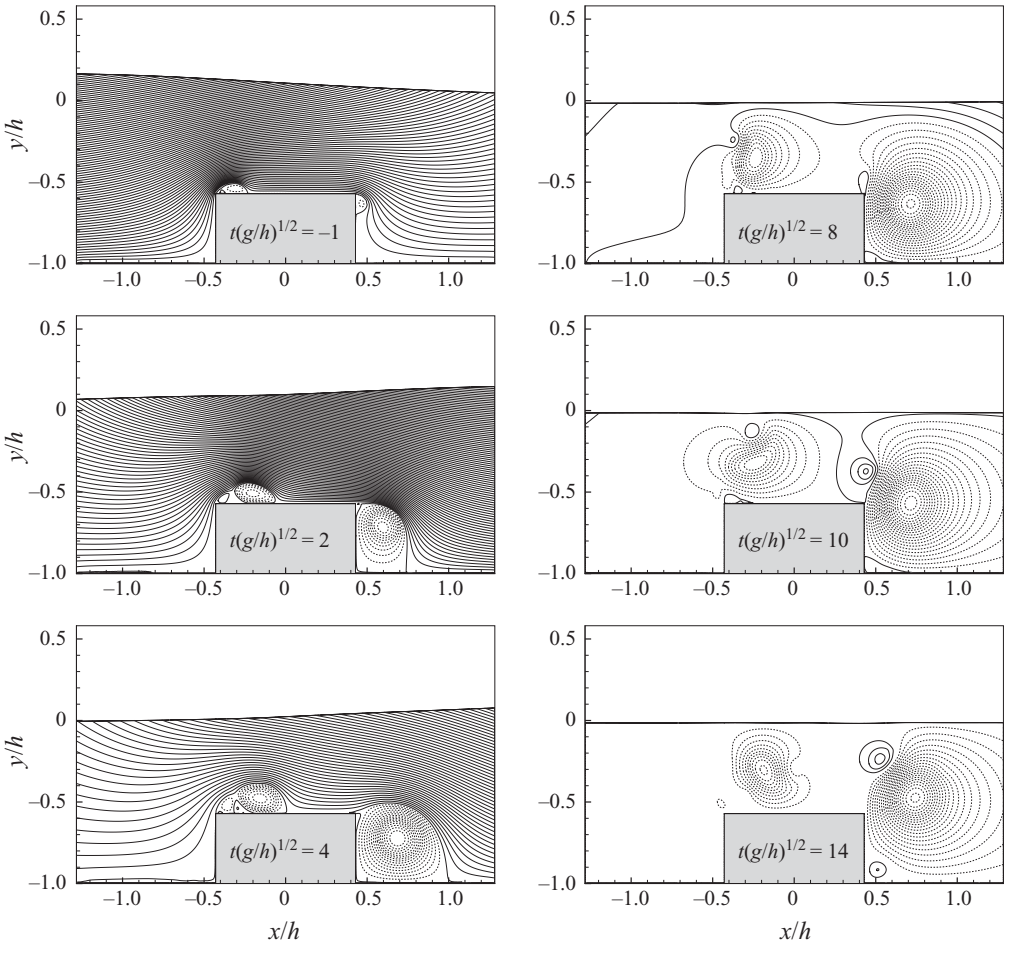


FIGURE 10. Evolution of the streamlines for $H/h = 0.17$.

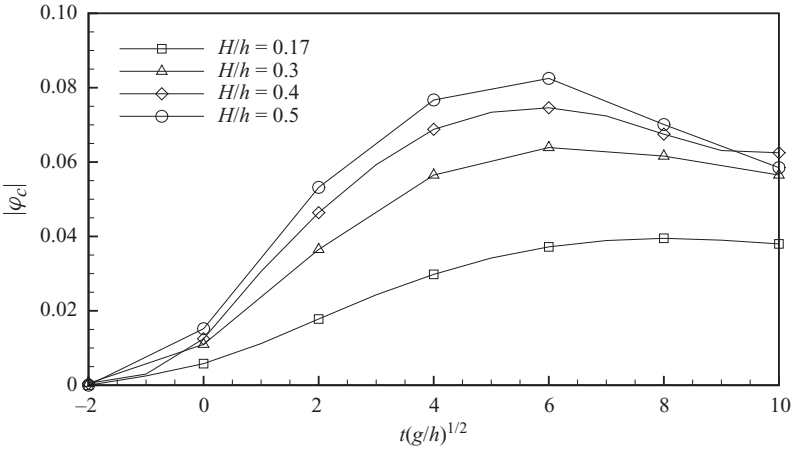


FIGURE 11. Time history of the maximum magnitude of the stream function in the core of the lee-side vortex for different wave heights.

https://doi.org/10.1017/S0022112010000145 Published online by Cambridge University Press

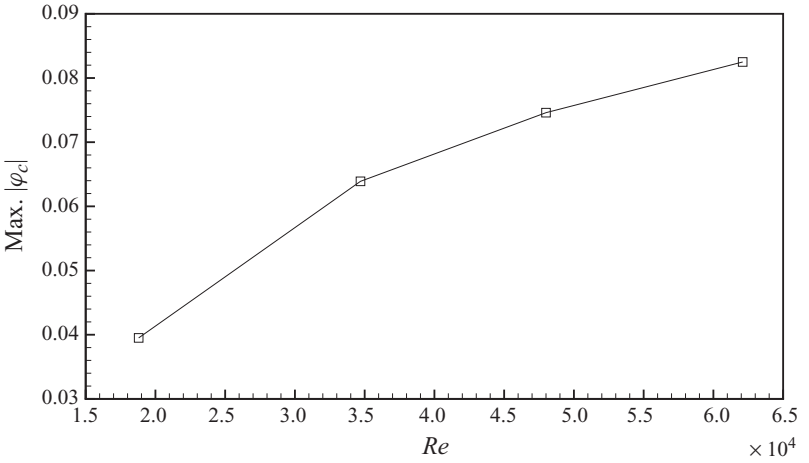


FIGURE 12. Maximum magnitude of the stream function in the core of the lee-side vortex as a function of the Reynolds number.

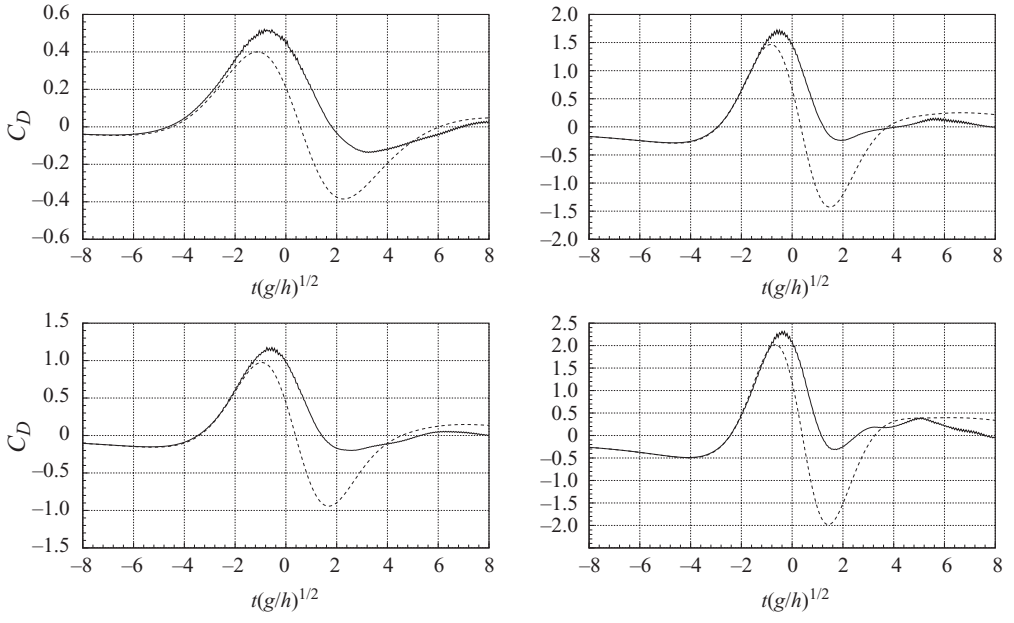


FIGURE 13. Comparison of the drag coefficient computed by ——, present model; - - -, potential-flow model.

In contrast to most previous numerical studies in this field (e.g. Tang & Chang 1998; Chang *et al.* 2001; Huang & Dong 2001), the results in this work reveal the detailed features of complicated vortex structures and agree satisfactorily with experimental observations. Results of this study elucidate the mechanisms of boundary layer separation and vortex shedding from structures submerged under solitary waves. The presented simulations also reveal that the effects of the generated vortices are preserved over a long period, and may cause local scouring of the foundation of submerged structures. As the wave height increases, the size and strength of the induced vortices increase. This phenomenon can be simply specified in terms of

https://doi.org/10.1017/S0022112010000145 Published online by Cambridge University Press

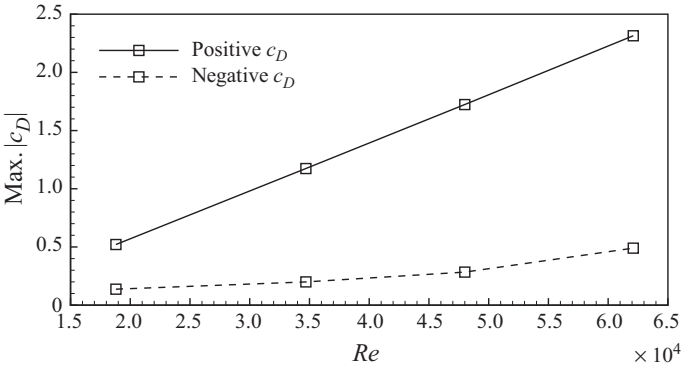


FIGURE 14. Maximum drag coefficient (positive and negative) versus the Reynolds number.

the H/h ratio. The bulging of the weather-side vortices on the obstacle changes the effective boundary of the flow above the submerged body, and may increase the height of the reflected waves and reduce the height of the transmitted wave. Although the solitary wave is almost preserved during which it propagates through the obstacle, the curve of the time history of the drag coefficient is asymmetric. This is mainly caused by the lee-side vortices, which act to 'pull' the obstacle in the positive x-direction.

This work was supported by the National Science Council of the Republic of China, Taiwan, under contract nos NSC92-2611-E-002-030 and NSC93-2611-E-002-012. M.-Y. L. would like to thank National Taiwan University for the post-doctoral fellowship award under contract no. 97R0044.

REFERENCES

BAKER, G. R., MEIRON, D. I. & ORSZAG, S. A. 1982 Generalized vortex methods for free-surface flow problems. *J. Fluid Mech.* **123**, 477–501.

BAKER, G. R., MEIRON, D. I. & ORSZAG, S. A. 1989 Generalized vortex methods for free surface flow problems. Part II. Radiating waves. *J. Sci. Comput.* **4** (3), 237–259.

CHANG, K. A., HSU, T. J. & LIU, P. L. F. 2001 Vortex generation and evolution in water waves propagating over a submerged rectangular obstacle. Part I. Solitary waves. *Coastal Engng* **44**, 13–36.

CHANG, K. A., HSU, T. J. & LIU, P. L. F. 2005 Vortex generation and evolution in water waves propagating over a submerged rectangular obstacle. Part II. Cnoidal waves. *Coastal Engng* **52**, 257–283.

COTTET, G. H. 1996 Artificial viscosity models for vortex and particle methods. *J. Comput. Phys.* **127**, 299–308.

DEGOND, P. & MAS-GALLIC, S. 1989 The weighted particle method for convection–diffusion equations. Part I. The case of isotropic viscosity; Part II. The anisotropic case. *Math. Comput.* **53**, 485–526.

GIRONELLA, X. & SÁNCHEZ-ARCILLA, A. 1999 Hydrodynamic behaviour of submerged breakwaters. Some remarks based on experimental results. In *Proceedings of Coastal Structures '99*, vol. 2, pp. 891–896. Santander, Spain.

GRILLI, S. T., LOSADA, M. A. & MARTIN, F. 1994 Characteristics of solitary wave breaking induced by breakwaters. *J. Waterw. Port Coast. Ocean Engng* **120** (1), 74–92.

GRUE, J. 1992 Nonlinear water wave at a submerged obstacle. *J. Fluid Mech.* **244**, 455–476.

GUYENNE, P. & NICHOLLS, D. P. 2005 Numerical simulation of solitary waves on plane slopes. *Math. Comput. Simul.* **69**, 269–281.

HSU, T. W., HSIEH, C. M. & HWANG, R. R. 2004 Using RANS to simulate vortex generation and dissipation around impermeable submerged double breakwaters. *Coastal Engng* **51**, 557–579.

https://doi.org/10.1017/S0022112010000145 Published online by Cambridge University Press

Huang, C. J. & Dong, C. M. 2001 On the interaction of a solitary wave and a submerged dike. *Coastal Engng* **43**, 265–286.

Idelsohn, S. R., Onate, E. & Sacco, C. 1999 Finite element solution of free-surface ship-wave problems. *Intl J. Numer. Methods Engng* **45**, 503–528.

Koumoutsakos, P., Leonard, A. & Pépin, F. 1994 Boundary conditions for viscous vortex methods. *J. Comput. Phys.* **113**, 52–61.

Lin, C., Chang, S., Ho, T. & Chang, K. 2006 Laboratory observation of solitary wave propagating over a submerged rectangular dike. *J. Engng Mech., ASCE* **132** (5), 545–554.

Lin, M.-Y. & Huang, L.-H. 2009 Study of water waves with submerged obstacles using a vortex method with Helmholtz decomposition. *Intl J. Numer. Methods Fluids* **60**, 119–148.

Lo, D. C. & Young, D. L. 2004 Arbitrary Lagrangian-Eulerian finite element analysis of free surface flow using a velocity-vorticity formulation. *J. Comput. Phys.* **195**, 175–201.

Mei, C. C. & Black, J. L. 1969 Scattering of surface waves by rectangular obstacles in waters of finite depth. *J. Fluid Mech.* **38**, 499–511.

Morino, L. 1990 Helmholtz and Poincaré potential-vorticity decompositions for the analysis of unsteady compressible viscous flows. In *Boundary Element Methods in Nonlinear Fluid Dynamics* (ed. P. K. Banerjee & L. Morino). Elsevier.

Ploumhans, P. & Winckelmans, G. S. 2000 Vortex methods for high-resolution simulations of viscous flow past bluff bodies of general geometry. *J. Comput. Phys.* **165**, 354–406.

Sánchez-Arcilla, A., Gironella, X., Verges, D., Sierra, J., Pena, C. & Moreno, L. 2000 Submerged breakwater and "bars": from hydrodynamics to functional design. In *Proceedings of the 27th International Conference on Coastal Engineering (ICCE'00)*. Sydney.

Sue, Y. C., Chern, M. J. & Hwang, R. R. 2005 Interaction of nonlinear progressive viscous waves with a submerged obstacle. *Ocean Engng* **32**, 893–923.

Sumer, B. M., Fredsøe, J., Lamberti, A., Zanuttigh, B., Dixen, M., Gislason, K. & Penta, A. F. D. 2005 Local scour at roundhead and along the trunk of low crested structures. *Coastal Engng* **52**, 995–1025.

Tanaka, M. 1986 The stability of solitary waves. *Phys. Fluids* **29**, 650.

Tang, C. J. & Chang, J. H. 1998 Flow separation during solitary wave passing over submerged obstacle. *J. Hydraul. Engng* **124**, 742–749.

Uhlman, J. S. 1992 An integral equation formulation of the equations of motion of an incompressible fluid. *Tech. Rep.* 10,086. Naval Undersea Warfare Center Division, Newport, Rhode Island.

Yeung, R. W. & Vaidhyanathan, M. 1992 Non-linear interaction of water waves with submerged obstacles. *Intl J. Numer. Methods Fluids* **14**, 1111–1130.

Zhang, D. H. & Chwang, A. T. 1999 On solitary waves forced by underwater moving objects. *J. Fluid Mech.* **389**, 119–135.

https://doi.org/10.1017/S0022112010000145 Published online by Cambridge University Press